

## **Texture-Aware Total Variation-Based Sun Glint Removal of Hyperspectral Images**

Duan, P.; Lai, J.; Kang, J.; Kang, X.; Ghamisi, Pedram; Li, S.;

Originally published:

July 2020

**ISPRS Journal of Photogrammetry and Remote Sensing 166(2020), 359-372**

DOI: <https://doi.org/10.1016/j.isprsjprs.2020.06.009>

Perma-Link to Publication Repository of HZDR:

<https://www.hzdr.de/publications/Publ-31967>

Release of the secondary publication  
on the basis of the German Copyright Law § 38 Section 4.

CC BY-NC-ND

# Texture-Aware Total Variation-Based Sun Glint Removal of Hyperspectral Images

Puhong Duan<sup>a</sup>, Jian Kang<sup>b</sup>, Xudong Kang<sup>a</sup>, Pedram Ghamisi<sup>c</sup>, Shutao Li<sup>a</sup>

<sup>a</sup>College of Electrical and Information Engineering, Hunan University, 410082 Changsha, China

<sup>b</sup>Faculty of Electrical Engineering and Computer Science, Technical University of Berlin, 10587 Berlin, Germany

<sup>c</sup>Helmholtz-Zentrum Dresden-Rossendorf, Helmholtz Institute Freiberg for Resource Technology, Freiberg 09599, Germany

---

## Abstract

Sun glint in hyperspectral images (HSIs) leads to undesirable spectral interference, which severely affects the subsequent image interpretation, such as the environmental monitoring of coastal areas. Sun glint removal methods aim at recovering a high quality image without sun glint from the original image. Most of methods mainly depend on an assumption that the near infrared band is strongly absorbed by water. However, this assumption is not always reliable because the infrared radiation in shallow or turbid water can be reflected back by the seabed or sediment, while it cannot be fully absorbed. Therefore, the reflected infrared radiation band still contains sun glint, and these methods cannot sufficiently remove the sun glint in HSIs. To address this problem, a texture-aware total variation (TATV)-based method is proposed to remove the sun glint of HSIs. The original HSI first is formulated as a desired clean image and a sun glint image. Then, in order to sufficiently remove the sun glint, we propose a variational model, where the different spectral characteristics of sun glint and other surrounding materials are considered. Specifically, we propose a texture-aware total variation regularized method to heavily penalize the variation of the sun glint areas. Experiments performed on simulated and real data sets demonstrate that our method can greatly outperform other state-of-the-art methods in removing sun glints.

*Keywords:* Hyperspectral image, sun glint removal, texture-aware total variation

---

## 1. Introduction

Nowadays, hyperspectral images (HSIs) can provide rich spectral information along with the high spatial resolution of the imaging scene. This excellent characterization makes such data very useful in solving practical problems [1–9], such as mapping bathymetry [10], water quality monitoring [11], and coral reef habitats [12]. However, owing to the specular reflection of solar radiation on non-flat water surface in the imaging process, the captured HSIs easily suffer from the contamination of the

---

*Email address:* xudong\_kang@163.com (Xudong Kang)

sun glints, which affects seriously the acquisition of underwater characteristics and the following image analysis.

Over the past decades, many sun glint methods have been proposed for multispectral images, which can be summarized into two categories [13–15], i.e., sea surface-based methods and band information-based methods. The sea surface-based methods are based on an assumption that the glint intensity is highly related to the probability distribution function of the wave slope, and then, to model a wind-speed dependent probability distribution function for the sea surface slope using aerial photographs of reflected sunlight. For example, Breon *et al.* analyzed a large set of reflectance measurements from glint-contaminated areas, and obtained the linear correlation between the wind speed and the mean square slope [16]. In [17], Fukushima *et al.* built a new linear relationship between the surface mean square slope and wind using radiance data, which can achieve a better fit in calm conditions. In [18], Ottaviani *et al.* proposed an improved atmospheric correction scheme to estimate the glint-corrected radiance via considering multiple scattering including aerosol, azimuth angle and wind speed. These methods mainly rely on the wind speed and wind direction to model the probability distribution of sea surface slopes. However, such prior knowledge cannot be easily obtained in practical applications.

The band information-based methods are based on an assumption that the water-leaving radiance in the near infrared (NIR) band is close to zero [1, 19, 20]. For example, in [21], Lyzenga *et al.* built the relationship among bands by using the covariance between each visible band and the NIR band. In [22], Goodman *et al.* introduced a wavelength-independent offset to correct each pixel, in which the band with wavelength 760nm was taken as the NIR band. In [23], Kutser *et al.* utilized the characteristic of the oxygen absorption band at 760nm to evaluate the size of the sun glint. These methods use the relationship between NIR and visible wavelengths to remove the contamination of sun glint. However, one main limitation of these methods is that the assumption may not be true for highly turbid environments [24]. To overcome the limitation, in [25], Harmel *et al.* exploited two short-wavelength infrared (SWIR) bands (centered on 1610 and 2190nm) to estimate the sun glint component of Sentinel-2 data, and then, the sun glint was removed from the top-of-atmosphere radiation over coastal and inland waters. Nevertheless, one limitation of this method is that it needs ancillary data about the atmospheric properties.

Considering the limitations of the previous methods, in this work, the original HSI  $\mathcal{S} \in \mathbb{R}^{P \times Q \times M}$  is modeled as a linear combination of the desired clean image  $\mathcal{X} \in \mathbb{R}^{P \times Q \times M}$  and the sun glint image  $\mathcal{Z} \in \mathbb{R}^{P \times Q \times M}$ , expressed as:  $\mathcal{S} = \mathcal{X} + \mathcal{Z}$ . The main aim of removing sun glint is to distinguish the sun glint-free image  $\mathcal{X}$  and the sun glint image  $\mathcal{Z}$  from an input hyperspectral image  $\mathcal{S}$ . This is an ill-posed inverse issue, which is able to be solved via introducing prior information. Therefore, from this perspective, the most important problem is how to design an effective prior knowledge, which is beneficial for cleaning the sun glint and restoring the sun glint-free image.

Currently, various image priors have been utilized in image processing problems. For example,

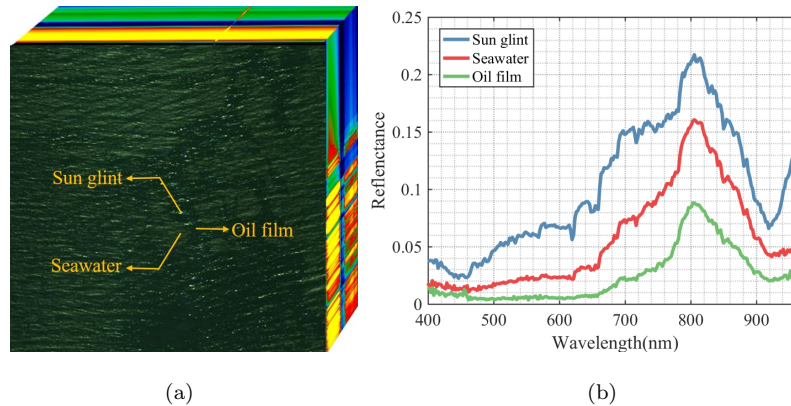


Fig. 1. A hyperspectral image and spectral curves of different objects.

in [26], He *et al.* used the low-rank prior of HSI to remove the mixed noise. In [27], Kang *et al.* adopted the smoothness prior of multipass InSAR, i.e., total variation (TV) norm, for deformation  
 45 monitoring. In [28], Dian *et al.* used the convolutional neural network to extract the prior information of the original image for pan-sharpening. In this paper, since the spectral reflectance value of the sun glint is always higher than one of the surrounding land covers [see Fig.1], the gradient values at the location of the sun glint becomes higher. Based on this observation, the TV prior is adopted in our method. Standard TV regularization imposes the same weights over the gradients of all the pixels.  
 50 Simply minimizing the corresponding total variation may not sufficiently remove the sun glint, since the variations of all the pixels are equally reduced.

To overcome this issue, in this work, we propose a texture-aware total variation (TATV) method for sun glint removal of HSIs, in which the texture information is incorporated into the TV model. This incorporation can enforce that the discriminative characteristics between land covers and sun glints  
 55 are maximal. The variations of sun glint areas are penalized with larger weights, so that the spectral values induced by sun glints can be significantly reduced. Experimental results also demonstrate that such modeling idea can more effectively remove the sun glint of HSIs with respect to previous methods. The main contributions of this paper are summarized as follows:

1) To the best of our knowledge, this is the first time to formulate the sun glint removal problem  
 60 as a variational optimization model. Different from previous methods, this model does not need any auxiliary data, such as wind speed or spectral range. The proposed model opens new opportunities for the challenging problem of sun glint removal.

2) We propose a texture-aware total variation method to remove sun glints, which can sufficiently decompose the original image into the sun glint image and the glint-free image for the downstream  
 65 tasks. For instance, the classification performance can be greatly improved on the glint-free image.

3) The alternating direction method of multiplier (ADMM) is adopted to solve the proposed model. Experimental results confirm that the proposed method can effectively remove the sun glint of HSIs

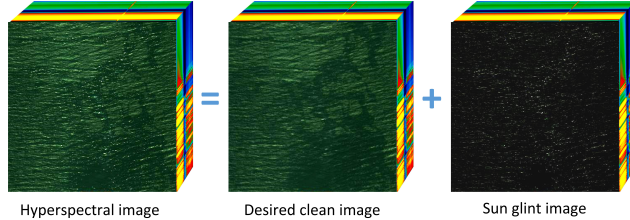


Fig. 2. Sun glint removal model of HSI.

with respect to other state-of-the-art techniques.

The rest of this paper is organized as follows. In Section 2, the proposed method is introduced in details, including the problem formulation and optimization. In Section 3, the experimental results on simulated and real datasets are described and discussed. Finally, the conclusions are presented in Section 4.

## 2. Proposed Method

In this section, the proposed TATV method is presented for sun glint removal of HSI.

### 2.1. Problem Formulation

As introduced before, an HSI  $\mathcal{S} \in \mathbb{R}^{P \times Q \times M}$ , where  $P$  and  $Q$  are the spatial dimension and  $M$  is the number of spectral bands, can be modeled as a linear superimposition of the desired clean image  $\mathcal{X}$  and sun glint image  $\mathcal{Z}$  [see Fig. 2]:

$$\mathcal{S} = \mathcal{X} + \mathcal{Z} \quad (1)$$

Our goal is to estimate the clean image  $\mathcal{X}$  with only  $\mathcal{S}$  known. Obviously, this is an ill-posed inverse problem, and has no unique solution. To solve this ill-posed problem, we need to use some prior information of the unknown  $\mathcal{X}$  and then add corresponding regularizer. In this work, one popular smoothness prior [29–31], i.e., total variation (TV) is adopted, which is extensively applied in many image processing problems, such as denoising, inpainting, and classification. The gradients of all the pixels are assigned with equal weight for calculating the TV term. The minimization based on it leads to an equal reduction of spectral values of sun glint and other areas. Although such operation can mitigate the spectral values of sun glints, the spectral information of other areas can be also lost. To address this issue, the texture information is imposed on the TV term, which can heavily penalize the variation values of the sun glint areas. Accordingly, the proposed optimization model can be represented as:

$$\mathcal{X} = \arg \min_{\mathcal{X}} \left\{ \frac{\mu}{2} \|\mathcal{S} - \mathcal{X}\|_F^2 + \eta \sum_m \|X_m\|_{TV} + \sum_m |S_m - X_m| \odot \|X_m\|_{TV} \right\} \quad (2)$$

90 where  $\|X\|_{TV} = \sum_i \|D_i x\|$  is the first-order difference of  $x$  in both horizontal and vertical directions at pixel  $i$ .  $\mathcal{S}$  is the original hyperspectral image, and  $\mathcal{X}$  is the resulting image.  $m$  represents the  $m$ th band.  $\mu$  and  $\eta$  denotes the weights. Thus, the objective function above can be described as:

$$\mathcal{X} = \arg \min_{\mathcal{X}} \left\{ \frac{\mu}{2} \|\mathcal{S} - \mathcal{X}\|_F^2 + \eta \sum_m \sum_i \|D_i x_m\|_2 + \sum_m \sum_i |s_{im} - x_{im}| \cdot \|D_i x_m\|_2 \right\} \quad (3)$$

## 2.2. Optimization

In order to solve the objective function, we consider an equivalent of (3) by introducing two auxiliary  
95 variables  $y_{im} = D_i x_{im}$  and  $\mathcal{Z} = \mathcal{S} - \mathcal{X}$ . Problem (3) can be converted into the following problem:

$$\mathcal{X} = \arg \min_{\mathcal{X}} \left\{ \frac{\mu}{2} \|\mathcal{Z}\|_F^2 + \sum_m \sum_i (\eta + |z_{im}|) \cdot \|y_{im}\|_2 \right\} \quad (4)$$

The optimization problem (4) can be solved by the ADMM framework [32–34], and Its augmented Lagrangian function is shown as follows:

$$L = \arg \min_{x, y, z} \left\{ \frac{\mu}{2} \|\mathcal{Z}\|_F^2 + \sum_m \sum_i (\eta + |z_{im}|) \cdot \|y_{im}\|_2 - \lambda_1^T (y_{im} - D_i x_m) + \frac{\beta_1}{2} \sum_m \sum_i \|y_{im} - D_i x_m\|_2^2 - \lambda_2^T (\mathcal{Z} - \mathcal{X} + \mathcal{S}) + \frac{\beta_2}{2} \|\mathcal{Z} - \mathcal{X} + \mathcal{S}\|_F^2 \right\} \quad (5)$$

where  $\lambda_1$  and  $\lambda_2$  are the Lagrange multipliers.  $\beta_1$  and  $\beta_2$  are the penalty parameters. The ADMM  
100 makes use of splitting one difficult optimization problem into several subproblems, where each of them has a closed-form solution. Accordingly, the minimization of  $L$  with respect to each variable can be solved by optimizing the following subproblems.

1) *y subproblem*: By fixing variables  $z$  and  $x$ , the optimization of  $L$  with respect to  $y$  in (5) can be written as:

$$\min_y \sum_m \sum_i (\eta + |z_{im}^k|) \cdot \|y_{im}\|_2 + \frac{\beta_1}{2} \sum_m \sum_i \left\| y_{im} - D_i x_m^k - \frac{\lambda_1}{\beta_1} \right\|_2^2 \quad (6)$$

Problem (6) is  $L_1$ -norm-induced subproblem, which can be easily solved via a soft thresholding method  
105 as

$$y_i^{k+1} = \mathcal{R}_\gamma(D_i x_m^k + \frac{\lambda_1}{\beta_1}) \quad (7)$$

where

$$\mathcal{R}_\gamma(\alpha) = \text{sign}(\alpha) \odot \max\{|\alpha| - \frac{\eta + |z_{im}^k|}{\beta_1}, 0\} \quad (8)$$

with  $\text{sign}(\cdot)$  and  $|\cdot|$  of a vector considered to be applied element-wise, and  $\odot$  representing element-wise product.

2) *z subproblem*: By fixing variables  $y$  and  $x$ , the optimization of  $L$  with respect to  $z$  in (5) can be  
110 written as:

$$\min_z \sum_m \sum_i (\eta + |z_{im}|) \cdot \|y_{im}^{k+1}\|_2 + \frac{\mu + \beta_2}{2} \left\| \mathcal{Z} - \frac{\beta_2}{\mu + \beta_2} (\mathcal{X}^k - \mathcal{S} + \frac{\lambda_2}{\beta_2}) \right\|_F^2 \quad (9)$$

Likewise, the subproblem can also be solved via soft thresholding method.

$$\mathcal{Z}^{k+1} = \max\left\{\frac{\beta_2}{\mu + \beta_2}(\mathcal{X}^k - \mathcal{S} + \frac{\lambda_2}{\beta_2}) - \frac{\|D\mathcal{X}^k\|_F}{\mu + \beta_2}, 0\right\} \odot \text{sgn}\left\{\frac{\beta_2}{\mu + \beta_2}(\mathcal{X}^k - \mathcal{S} + \frac{\lambda_2}{\beta_2})\right\} \quad (10)$$

3) *x subproblem*: By fixing variables  $y$  and  $z$ , the optimization of  $L$  with respect to  $x$  in (5) can be written as:

$$= \min_x \frac{\beta_1}{2} \sum_m \sum_i \left\| y_{im}^{k+1} - D_i x_m - \frac{\lambda_1}{\beta_1} \right\|_2^2 + \frac{\beta_2}{2} \left\| \mathcal{Z}^{k+1} - \mathcal{X} + \mathcal{S} - \frac{\lambda_2}{\beta_2} \right\|_F^2 \quad (11)$$

The solution of subproblem (11) can be obtained by calculating the derivative of (11) with respect to  $x$  and setting it as zero. Then, we can obtain the following equation:

$$(\beta_1 D^T D + \beta_2)x = \beta_1 D^T (y^{k+1} - \frac{\lambda_1}{\beta_1}) + \beta_2 (\mathcal{Z}^{k+1} - \mathcal{S} - \frac{\lambda_2}{\beta_2}) \quad (12)$$

Owing to the block-circulant structure of the matrix  $D^T D$ , the inverse problem can be solved by 2D Fourier Transform and its inverse transform [35]. We can obtain the solution of  $x^{k+1}$ :

$$\mathcal{F}^{-1}\left\{\frac{\mathcal{F}(\beta_1 D^T (y^{k+1} - \lambda_1/\beta_1) + \beta_2 (\mathcal{Z}^{k+1} + \mathcal{S} - \lambda_2/\beta_2))}{\beta_1 \mathcal{F}^*(D) \odot \mathcal{F}(D) + \beta_2}\right\} \quad (13)$$

where  $\mathcal{F}$  denotes the 2D discrete Fourier transform. “\*” represents the conjugate.

4) *Update Lagrange Multipliers*: Before stepping into the next iteration, all Lagrange multipliers must be updated:

$$\begin{aligned} \lambda_1^{k+1} &= \lambda_1^k - \beta_1 (y^{k+1} - D x^{k+1}) \\ \lambda_2^{k+1} &= \lambda_2^k - \beta_2 [\mathcal{Z}^{k+1} - (\mathcal{X}^{k+1} - \mathcal{S})] \end{aligned} \quad (14)$$

The proposed RATV method for sun glint removal of HSIs is summarized in **Algorithm 1**.

---

**Algorithm 1** RATV for sun glint removal of HSIs

---

**Input:**  $\mathcal{S}, \mu, \eta$

1: Initialize  $\lambda_1^{(0)} = \lambda_2^{(0)} = 0$

2: **For**  $k = 0$  to  $k_{max}$  **do**

3:     Update  $y^{k+1}$  via Eq. (7)

4:     Update  $z^{k+1}$  via Eq. (10)

5:     Update  $x^{k+1}$  via Eq. (13)

6:     Update  $\lambda^{k+1}$  via Eq. (14)

7: **End For**

**Output:**  $\mathcal{X}$

---

### 3. Experiments

In this section, experiments performed on the simulated and real data sets are presented. In order to better demonstrate the superiority of the proposed method, six state-of-the-art methods are adopted

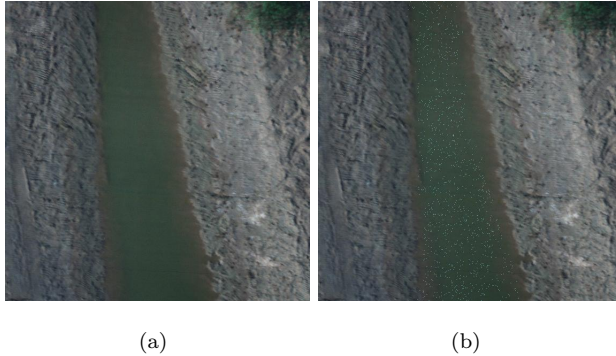


Fig. 3. Three bands composite of the Simulated data set. (a) Clean image. (b) Contaminated image by sun glint.

125 for comparison, including three sun glint removal methods, and three hyperspectral denoising methods, i.e., Lyzenga’s method [21], Goodman’s method [22], Kutser’s method [23], total variation-regularized low rank matrix factorization (LRTV) [36], hyperspectral mixed Gaussian and sparse noise reduction method (HyMiNoR) [37], and non-i.i.d. low-rank matrix factorization model with Bayesian framework (LRMFBF)[38]. For the parameters of these methods, we carefully followed the authors’ suggestions  
 130 in the corresponding papers to obtain optimal results.

### 3.1. Data sets

1) Simulated data set: In order to objectively evaluate the performance of the proposed method, we use a clean data set for the simulated experiment. This data set has  $561 \times 570$  pixels in the spatial domain, and consists of 270 spectral bands from 0.4 to 1  $\mu\text{m}$ . To simulate the complicated sun glint  
 135 case in a real scene, a real sun glint pixel is selected from the contaminated data set, and then, 1000 pixels chosen randomly from the water region of the clean data set are replaced with the sun glint pixel. Fig. 3 shows the clean image and the simulated image.

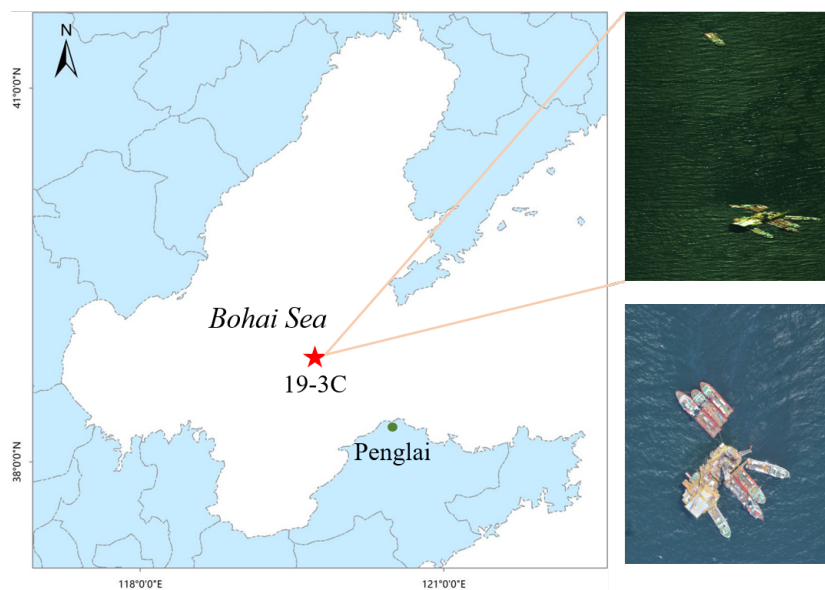
2) Real data sets: In order to validate the effectiveness of the proposed method, several real hyperspectral data sets, i.e., Penglai, YellowRiver-1, YellowRiver-2, and YellowRiver-3, are employed  
 140 in the following experiments. These data sets are from two types of hyperspectral sensors, in which YellowRiver-1, YellowRiver-2, and YellowRiver-3 data sets were captured from the same hyperspectral sensors with different flight routes.

The Penglai data set was acquired by the AISA+ hyperspectral sensor on August 23, 2011 over the Penglai 19-3 C platform oil field located in China Bohai Sea, which was a serious oil spill accident.  
 145 This image has 258 spectral bands from 0.4 to 0.97  $\mu\text{m}$ , and its spatial size is  $610 \times 340$ . Fig. 4 shows the location of the oil spill and the AISA+ hyperspectral image. Detailed information about the AISA+ hyperspectral sensor is shown in Table 1.

Other three data sets, i.e., YellowRiver-1, YellowRiver-2, and YellowRiver-3, were all acquired by

Table 1. Detailed information about AISA+ hyperspectral sensor.

Parameters	Index
Number of bands	258
Spectral range	400-970nm
Spectral resolution	2.3nm/pixel
Spatial size	800*450
Field of view	39.7°
Instantaneous field of view	0.078



(a)

Fig. 4. Location of the oil spill and hyperspectral image of Penglai.

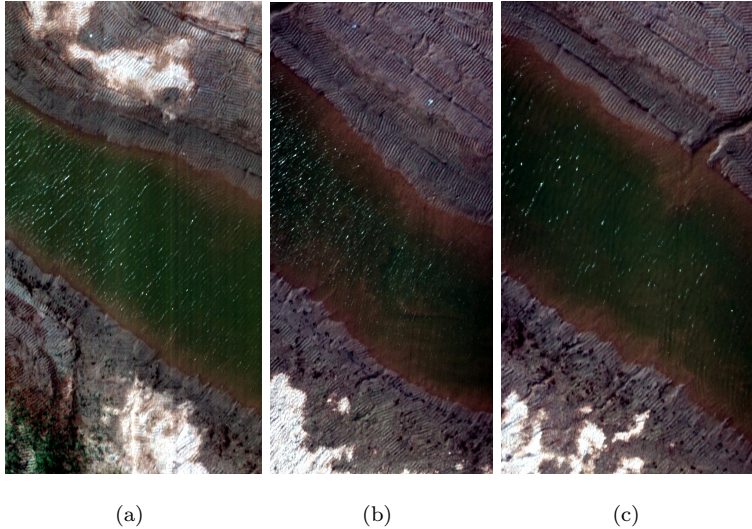


Fig. 5. False color composite images of different regions: (a) YellowRiver-1 image, (b) YellowRiver-2 image, and (c) YellowRiver-3 image.

the Headwall hyperspectral sensor over the Yellow River located in China, Ying Dong city. They have  
 150 270 spectral bands from 0.4 to 1  $\mu\text{m}$ . All the three data are contaminated by sun glint with different intensities. Detailed information about the Headwall hyperspectral sensor is shown in Table 2. Fig. 5 shows the color composite images.

Table 2. Detailed information about Headwall hyperspectral sensor.

Parameters	Index
Number of bands	270
Spectral range	400-1000nm
Spectral resolution	2.2nm/pixel
Field of view	33°
Instantaneous field of view	0.9

### 3.2. Parameter settings

In the proposed TATV method, the selection of parameters, i.e.,  $\mu$  and  $\eta$ , affects the performance  
 155 of sun glint removal. Therefore, the influence of these parameters on the performance is analyzed. Fig. 6 shows the contour plots of the PSNR and MSAM with respect to  $\mu$  and  $\eta$ . It can be seen from Fig. 6 (a) that the proposed method obtains the highest value when  $\mu = 2$  and  $\eta = 0.015$ . Moreover, when  $\mu$  and  $\eta$  are relatively small or large, the performance of the proposed method tends to decrease. Furthermore, the same tendency can also be found in Fig. 6 (b). Therefore, in this work, the default

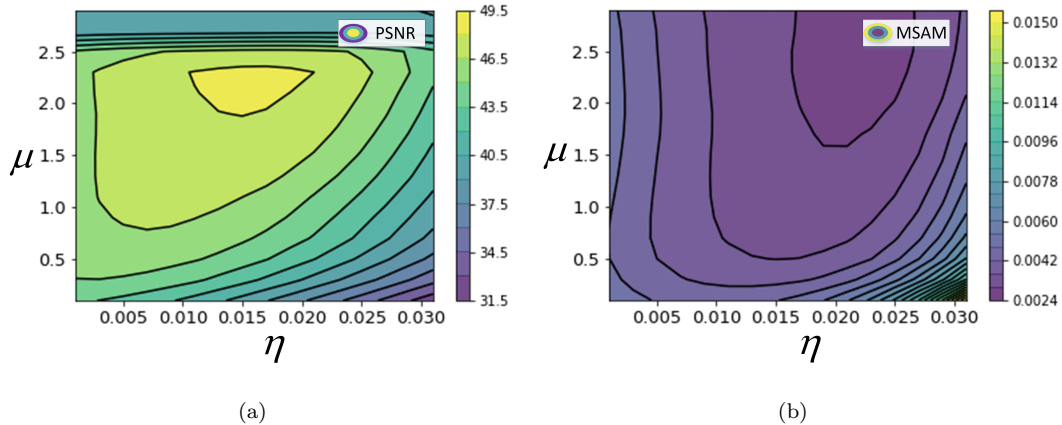


Fig. 6. The influence of different parameters on the performance of the proposed method.

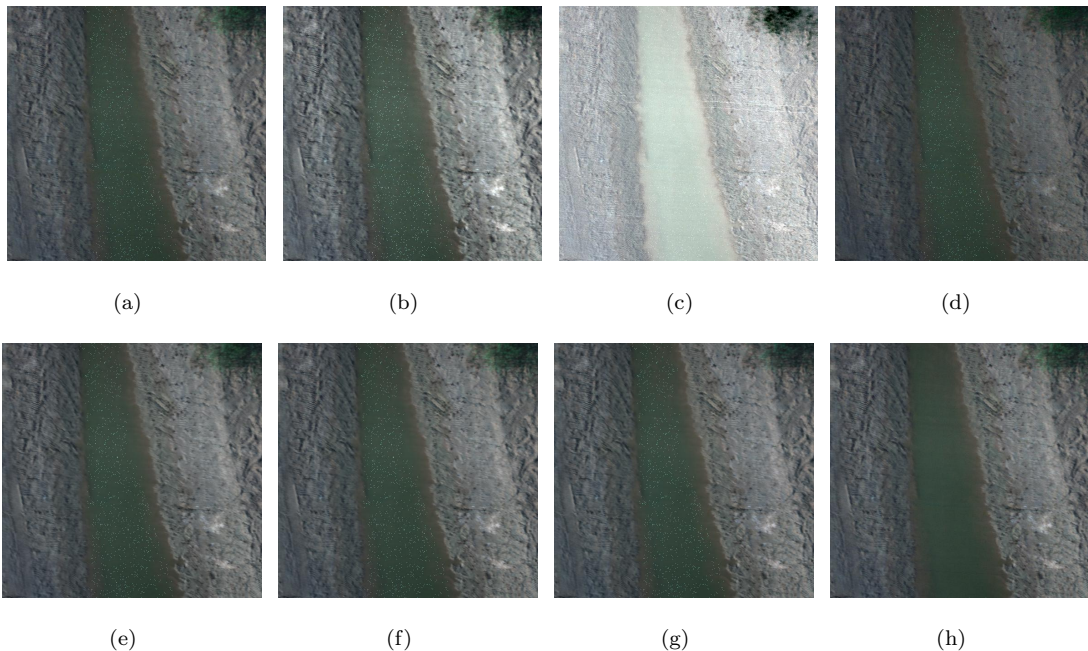


Fig. 7. Simulated image before and after removing sun glint. (a) Original image (R:124,G:65,B:37). (b) Lyzenga *et al.* method [21]. (c) Goodman *et al.* method [22]. (d) Kutser *et al.* method [23]. (e) LRTV method [36]. (f) HyMiNoR method [37]. (g) LRMFBF method [38]. (h) Our method.

160 parameters settings are set as  $\mu = 2$  and  $\eta = 0.015$ . The following experiments have demonstrated that the proposed method is able to obtain satisfactory performance with this parameter setting.

### 3.3. Simulated experiment

To evaluate objectively the performance of all studied methods, two widely used quantitative indexes are adopted, i.e., the peak signal-to-noise ratio (PSNR) and mean spectral angle mapper (MSAM) [36]. In the objective results, the PSNR result is the average value of those on all spectral  
165

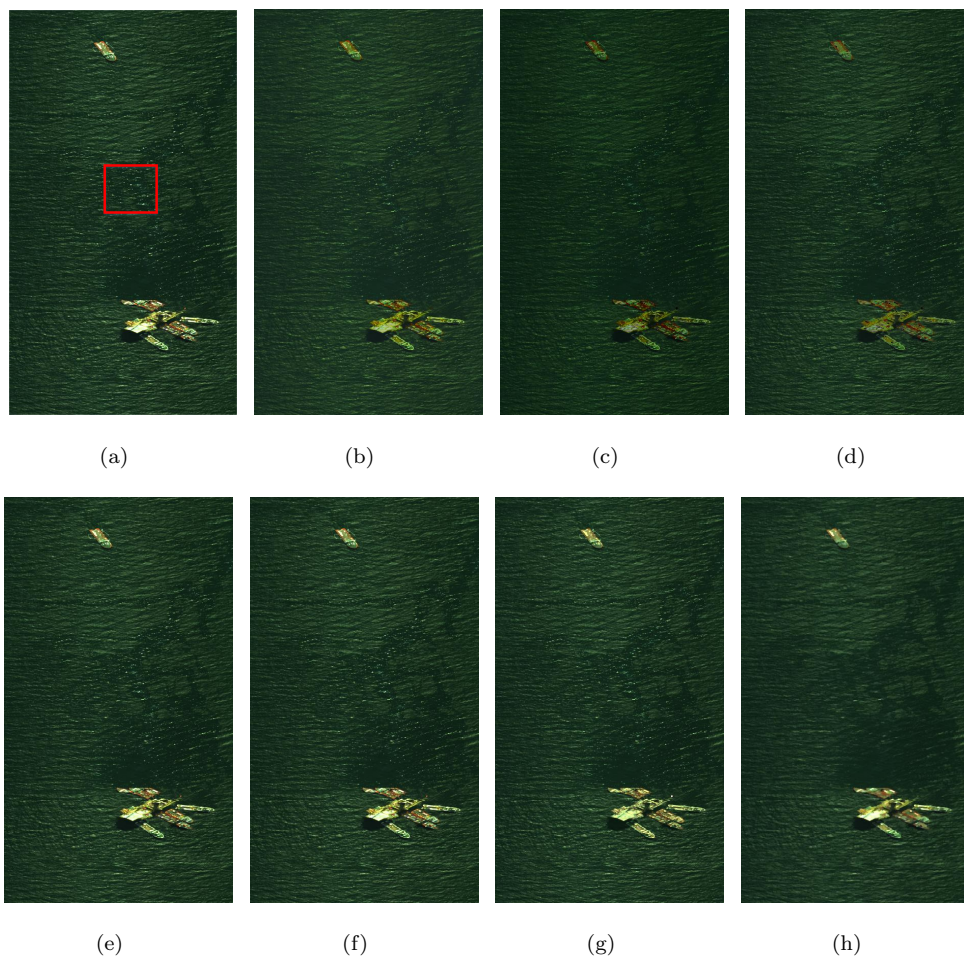


Fig. 8. Penglai image before and after removing sun glint. (a) Original false-color image (R:140, G:180, B:220). (b) Lyzenga *et al.* method [21]. (c) Goodman *et al.* method [22]. (d) Kutser *et al.* method [23]. (e) LRTV method [36]. (f) HyMiNoR method [37]. (g) LRMFBF method [38]. (h) Our method.

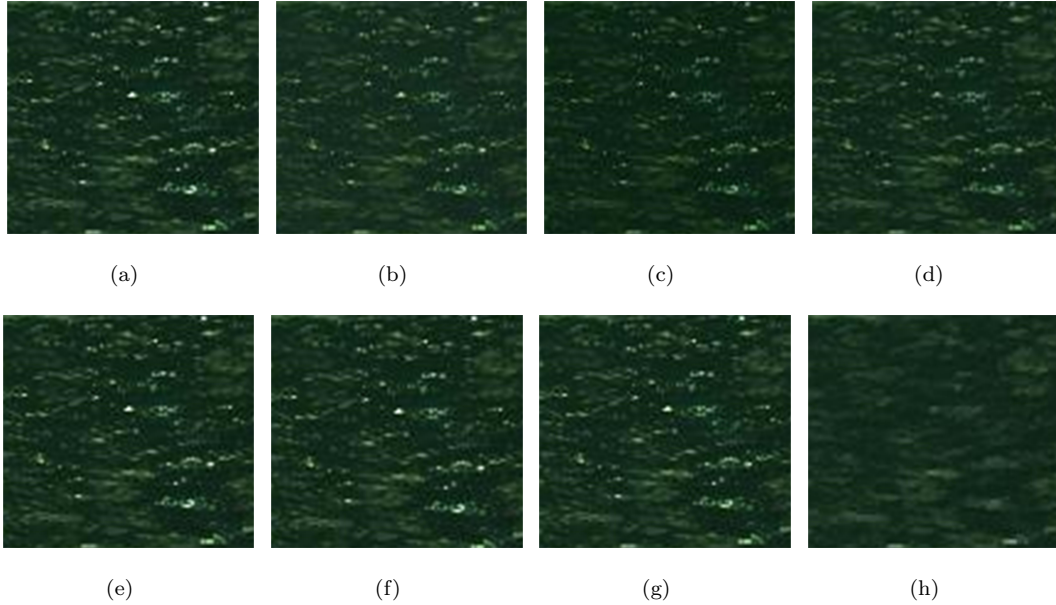


Fig. 9. Magnified results from Fig. 8. (a) Original false-color image (R:140, G:180, B:220). (b) Lyzenga *et al.* method [21]. (c) Goodman *et al.* method [22]. (d) Kutser *et al.* method [23]. (e) LRTV method [36]. (f) HyMiNoR method [37]. (g) LRMFBF method [38]. (h) Our method.

bands. Higher values indicate better performances. For the MSAM index, the lower values represent a better quality.

Fig. 7 presents the visual comparison of all studied methods. As shown in this figure, all denoising methods, i.e., LRTV, HyMiNoR, and LRMFBF, cannot completely eliminate the sun glint in the presented results. The reason is that these TV terms are constructed for removing mixed noise. For sun glint methods, they also yield the similar results, since the assumption used in these methods are not hold in the complex scene. Compared to other methods, it can be clearly seen that our method can effectively remove the sun glint in the contaminated water, and also well preserve the spatial details of land covers. Besides, Table 3 shows the quantitative assessment of all compared methods. It can be seen that our method outperforms other studied methods in terms of all quality indexes, which also indicates the superiority of our method.

Table 3. Objective comparison of different methods on the simulated data set. The highlighted bold value of each index represents the highest value among all studied methods.

Indexes	Lyzenga	Goodman	Kutser	LRTV	HyMiNoR	LRMFBF	Our method
PSNR	19.474	7.835	23.857	31.435	31.277	31.055	<b>48.512</b>
MSAM	0.135	0.294	0.088	0.085	0.096	0.099	<b>0.028</b>

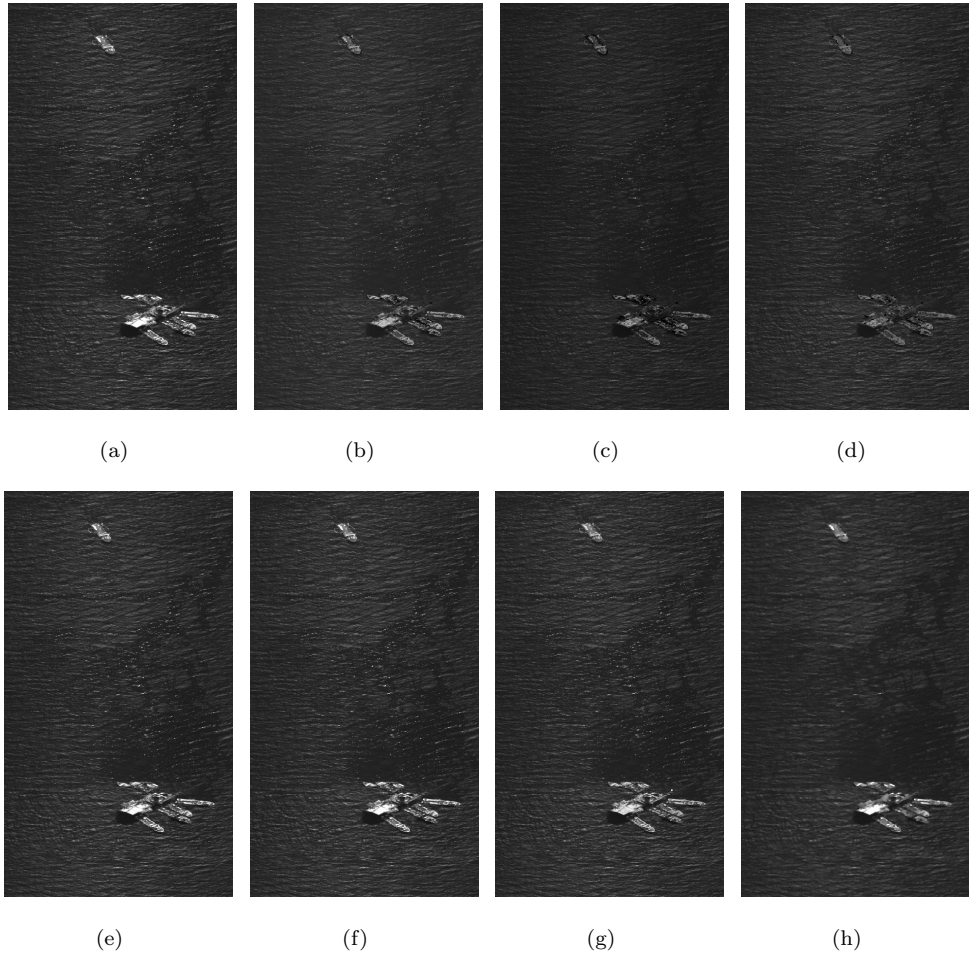


Fig. 10. Penglai image before and after removing sun glint. (a) Original image of band 200. (b) Lyzenga *et al.* method [21]. (c) Goodman *et al.* method [22]. (d) Kutser *et al.* method [23]. (e) LRTV method [36]. (f) HyMiNoR method [37]. (g) LRMFBF method [38]. (h) Our method.

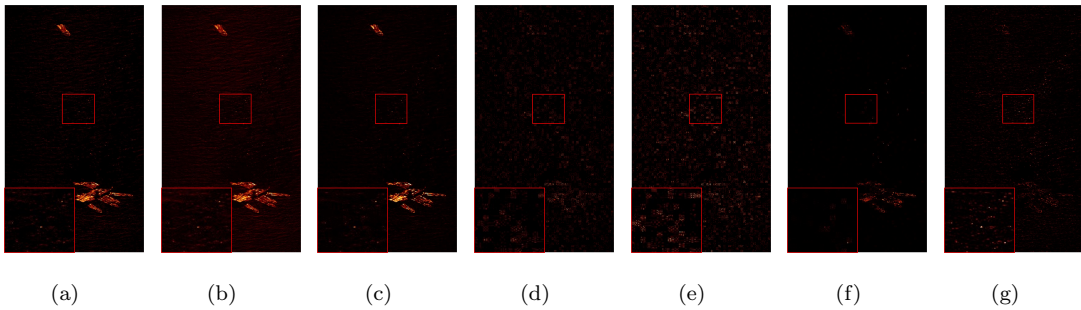


Fig. 11. Difference images between the source band 200 and the resulting images on Penglai image. (a) Lyzenga *et al.* method [21]. (b) Goodman *et al.* method [22]. (c) Kutser *et al.* method [23]. (d) LRTV method [36]. (e) HyMiNoR method [37]. (f) LRMFBF method [38]. (g) Our method.

### 3.4. Experiments on real data sets

The first experiment is performed on Penglai data set. This image is contaminated by the sun glint because of the specular reflection of light from the oil spill areas. Fig. 8 (a) shows the false-color composite image, and Fig. 8 (b)-(h) presents the resulting images of different methods. As shown in this figure, it can be seen that the Lyzenga’s method only can slightly remove the sun glint in the original image, but leave heavy sun glint in the experimental result. The reason is that the relationship between each band and the NIR band cannot be modeled well by the covariance. For the Goodman’s method, it suppresses the specular reflection of the entire image. However, it still cannot remove the sun glint, since the assumption about zero water-leaving radiance in the NIR region of spectrum is not hold in the sea surface corrupted by the oil spill. For the Kutser’s method, the sun glint in the original image still cannot be removed because it also assumes that the water-leaving radiance in the NIR band is negligible. The denoising methods, i.e., LRTV, HyMiNoR, and LRMFBF, do not work appropriately in removing sun glint. This is mainly because the regularization term of those denoising approaches fails to smooth out the sun glint. The denoising methods are targeted for noise removal, where the corresponding penalty terms are designed based on the prior knowledge of the noise. However, the structural information like sun glint cannot be modeled well by these methods. By contrast, the proposed method can achieve better performance in removing the sun glint than other methods.

In addition, the magnified results of Fig. 8 are shown in Fig. 9. It can be clearly seen that the Goodman’s method can more or less remove the sun glint, but the performance is not satisfactory. The Kuster’s method obtains the similar result. Three mixture denoising methods including LRTV, HyMiNoR, and LRMFBF fail to remove the sun glint. From these figures, it can be observed that the proposed TATV method can produce the best performance in removing sun glint.

Fig. 10 presents the results of different approaches before and after removing sun glint from band 200. To clearly evaluate the performance of different approaches in terms of removing sun glint, Fig. 11 displays the difference images between the original band 200 and the resulting band obtained by different methods. By comparing the resulting images of different methods, several observations can be easily obtained from both Figs. 10 and 11. First, the three sun glint methods, to some extent, can suppress the sun glint with low intensity [see Fig. 10 (b)-(d)]. They also remove the main structures of land covers such as the ‘working ship’[see Fig. 11 (a)-(c)]. Second, all denoising methods fail to restore the desired clean image from the sun glint-contaminated image. Specifically, from the Fig. 11 (d)-(f), it can be seen that there are very little information in the difference images, which illustrates that the difference between band 200 and each result is relatively small. Third, it is not hard to see that the proposed TATV method can effectively remove sun glint [see Fig.10 (h)] and better preserve the spatial structure of the original image [see Fig.11 (g)].

The second experiment is tested on YellowRiver data set. There are heavy contamination of sun

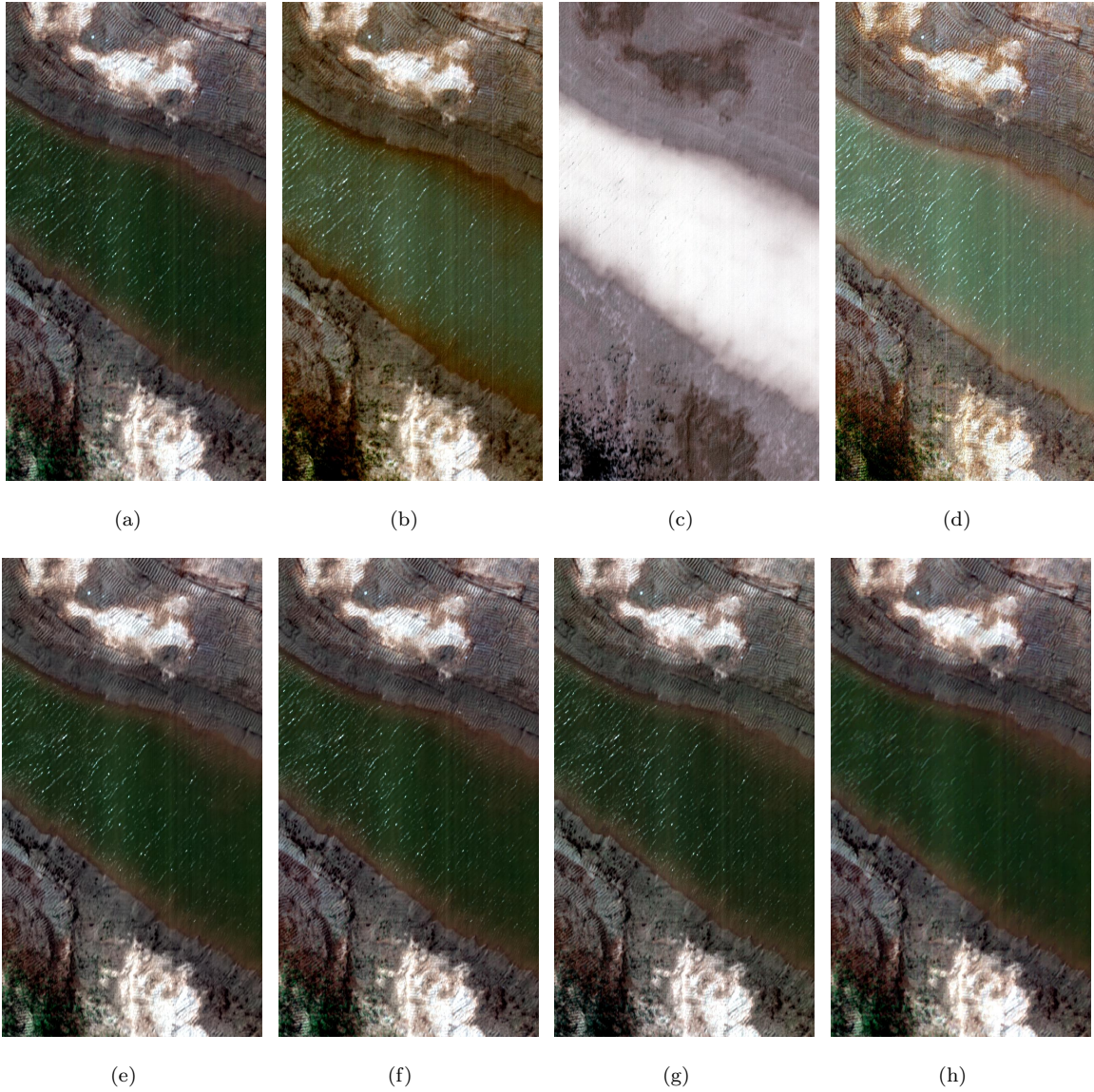


Fig. 12. YellowRiver-1 image before and after removing sun glint. (a) Original false-color image (R:124, G:65, B:37). (b) Lyzenga *et al.* method [21]. (c) Goodman *et al.* method [22]. (d) Kutser *et al.* method [23]. (e) LRTV method [36]. (f) HyMiNoR method [37]. (g) LRMFBF method [38]. (h) Our method.

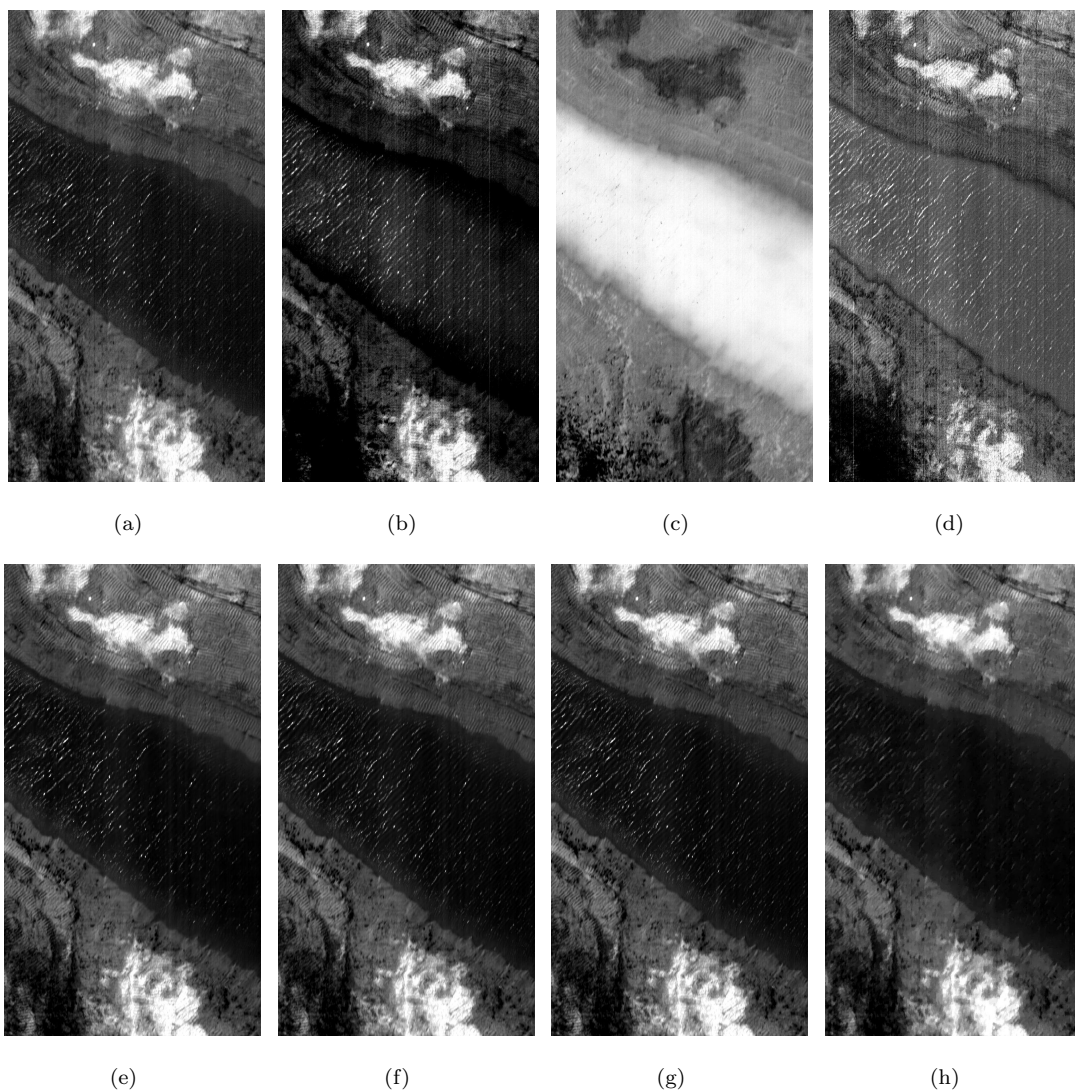


Fig. 13. YellowRiver-1 image before and after removing sun glint. (a) Original image of band 20. (b) Lyzenga *et al.* method [21]. (c) Goodman *et al.* method [22]. (d) Kutser *et al.* method [23]. (e) LRTV method [36]. (f) HyMiNoR method [37]. (g) LRMFBF method [38]. (h) Our method.

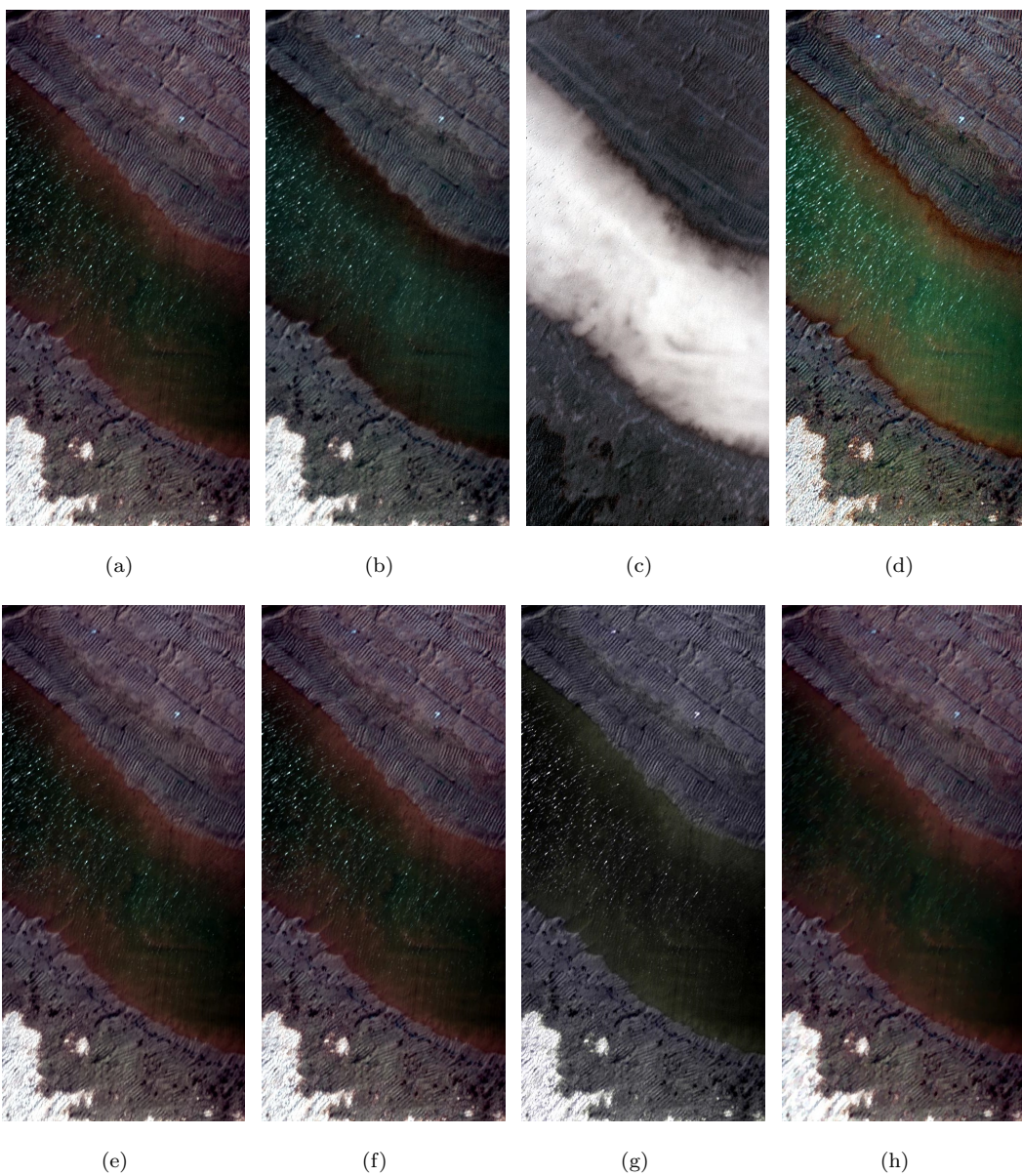


Fig. 14. YellowRiver-2 image before and after removing sun glint. (a) Original false color image (R:124, G:65, B:37). (b) Lyzenga *et al.* method [21]. (c) Goodman *et al.* method [22]. (d) Kutser *et al.* method [23]. (e) LRTV method [36]. (f) HyMiNoR method [37]. (g) LRMFBF method [38]. (h) Our method.

glint in the Yellow River region. Fig. 12 presents the false-color composite image of three bands before and after removing sun glint. In this figure, Goodman’s method does not work, and distorts the spectral-spatial information. This is mainly because the assumption that the reflectance at 750nm is equal to a constant may be not true for this image captured by the headwall sensor. For Lyzenga’s method, it still cannot remove the sun glint. A similar phenomenon also appears in Kuster’s method. The reason is that current methods for correcting sun glint generally rely on the NIR band-based information to assessing the sun glint contamination level. However, for the complex water environment, this assumption may be not reliable, which causes the performance to be unsatisfactory. Three denoising methods still cannot remove the sun glint in the water area because the regularization term is designed to remove mixture noise. Different from other methods, the proposed TATV method still can better remove the sun glint and preserve the spatial details of land covers.

In addition, Fig. 13 presents the resulting images of different methods for band 20 of YellowRiver-1 image. As shown in this figure, it can be observed that all compared methods cannot eliminate the sun glint in the original image. In comparison, the proposed method achieves better visual performance.

The third experiment is performed on YellowRiver-2 data set. In Fig.14 (a), the contaminated three-channel image is composed of the 124th, 65th, and 37th bands. In this example, it can be seen from Fig.14 (b)-(d) that three methods about sun glint removal still fail to correct the sun glint. This is due to the fact that these methods depend on the assumption that all near-infrared radiation is absorbed by water, and thus, the water-leaving radiance is close to zero. In practice, however, the infrared radiation has been reflected into the air in turbid water. For three denoising methods, since the TV-terms are designed to smooth image mixture noise, these methods cannot restore the desired clean image. Based on the visual comparison in Fig. 14, the proposed method can generate the better visual performance in removing the sun glint and preserving the details.

The fourth experiment is performed on YellowRiver-3 data set. As before, the same phenomenon can be observed in Fig.15. Our method still provides the best performance compared to other methods. The main reason is that the texture-aware TV term is able to well discriminate the sun glint and water body.

### 3.5. Classification Performance

In this subsection, in order to demonstrate the effectiveness of the sun glint removal approaches for the land cover classification, a spectral classifier, i.e., support vector machine (SVM) [39, 40], is utilized to assess the accuracies of different resulting images. The SVM classifier is implemented with the LIBSVM library, in which the radial basis function kernel with fivefold cross-validation is adopted. Four widely used objective metrics, i.e., the overall accuracy (OA), the average accuracy (AA), the kappa coefficient, and the class individual accuracy (CA), are used to evaluate the classification performance. OA denotes the percentages of correctly classified pixels. AA indicates the mean of the percentage of correctly classified pixels for each class. kappa coefficient represents the percentage of correctly

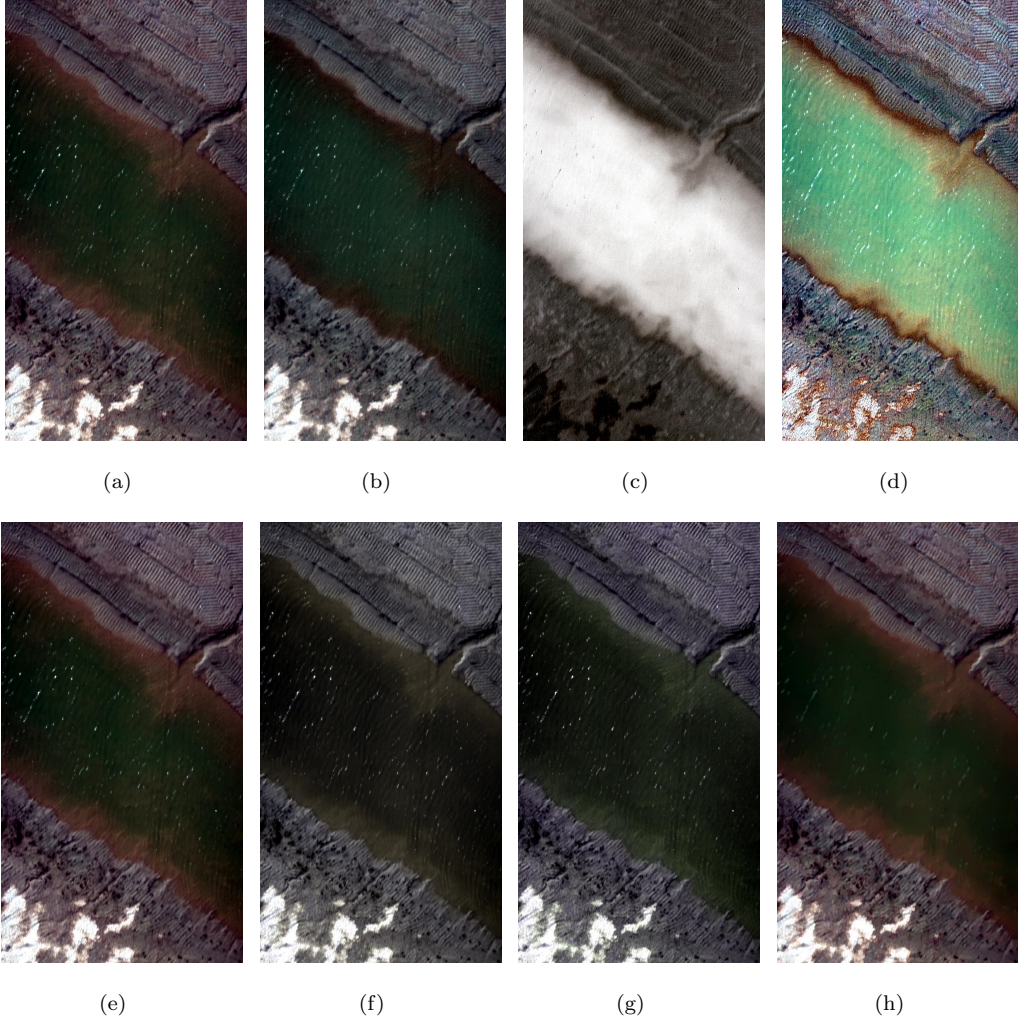


Fig. 15. YellowRiver-3 image before and after removing sun glint. (a) Original false color image (R:124, G:65, B:37). (b) Lyzenga *et al.* method [21]. (c) Goodman *et al.* method [22]. (d) Kutser *et al.* method [23]. (e) LRTV method [36]. (f) HyMiNoR method [37]. (g) LRMFBF method [38]. (h) Our method.

classified pixels corrected by the number of agreements. CA calculates the percentage of correctly  
 250 classified pixels for each class.

The experiment is performed on the Penglai data set. The oil spill region of this image is contaminated by the sun glint. Therefore, when the sun glint is removed, the accuracy of oil spill detection will be increased. To a certain extent, this experiment also demonstrates the effectiveness of different sun glint removal methods. Fig. 16 shows the comparative results obtained by different methods. The  
 255 reference data of this image consists of 3 classes. The training samples which account for 1% of the reference data are selected randomly, and the remaining samples are used as the test set. It can be seen from Fig. 16 that other studied methods produce many noise-like mislabeled pixels in the oil spill region. Different from these approaches, our method yields a smoother visual appearance in oil spill region. The main reason is that the proposed method can better remove the sun glint in the oil  
 260 spill region. Furthermore, our method provides the highest OA reported in Table 4, and the detection accuracy of the oil spill region is also increased by 5.5%.

Table 4. Classification accuracies of the SVM classifier on the different resulting images, i.e., Raw Data, Lyzenga *et al.* [21], Goodman *et al.* [22], Kuster *et al.* [23], LRTV [36], HyMiNoR [37], LRMFBF [38] and our method, respectively. Numbers in the parenthesis represents the standard variances of the accuracies obtained in 10 repeated experiments.

Classes	Raw data	Lyzenga	Goodman	Kutser	LRTV	HyMiNoR	LRMFBF	Our method
Seawater	97.30(0.12)	97.17(0.12)	97.17(0.14)	97.22(0.16)	97.71(0.17)	97.40(0.14)	96.12(0.17)	<b>98.13(0.16)</b>
Oil film	69.59(1.13)	69.24(1.25)	67.98(1.17)	69.86(1.35)	71.31(1.77)	68.68(1.04)	68.67(1.05)	<b>73.42(0.91)</b>
Working ship	66.48(5.12)	67.79(6.36)	63.84(8.02)	68.98(4.27)	66.10(6.25)	<b>69.53(7.25)</b>	61.37(4.13)	63.24(5.64)
OA	89.26(0.38)	89.11(0.41)	88.49(0.19)	89.41(0.41)	90.04(0.56)	89.05(0.33)	88.26(0.43)	<b>90.86(0.35)</b>
AA	77.79(1.62)	78.07(2.0)	76.33(2.35)	<b>78.69(1.28)</b>	78.37(1.90)	78.54(2.23)	75.39(1.50)	78.26(1.93)
Kappa	72.41(0.75)	72.00(0.81)	70.70(0.39)	72.68(0.85)	74.35(1.22)	72.01(0.69)	69.53(0.84)	<b>76.41(0.70)</b>

### 3.6. Analysis of Computational Complexity

The complexities of the proposed TATV method are shown below item by item (the numbers between the parentheses show the corresponding equation):

- 265 • (7):  $\mathcal{O}(PQM)$ .
- (10):  $\mathcal{O}(PQM)$ .
- (13):  $\mathcal{O}(PQM \log(PQ)) + \mathcal{O}(PQM)$ .

Among three steps of the TATV method, (13) dominates the computational complexity of the proposed method. Therefore, the complexity of the proposed method is  $\mathcal{O}(K(PQM \log(PQ)) + \mathcal{O}(PQM))$ , where  
 270  $K$  denotes the total number of the iterations. In this work,  $K$  is set to be 40 for all experiments.

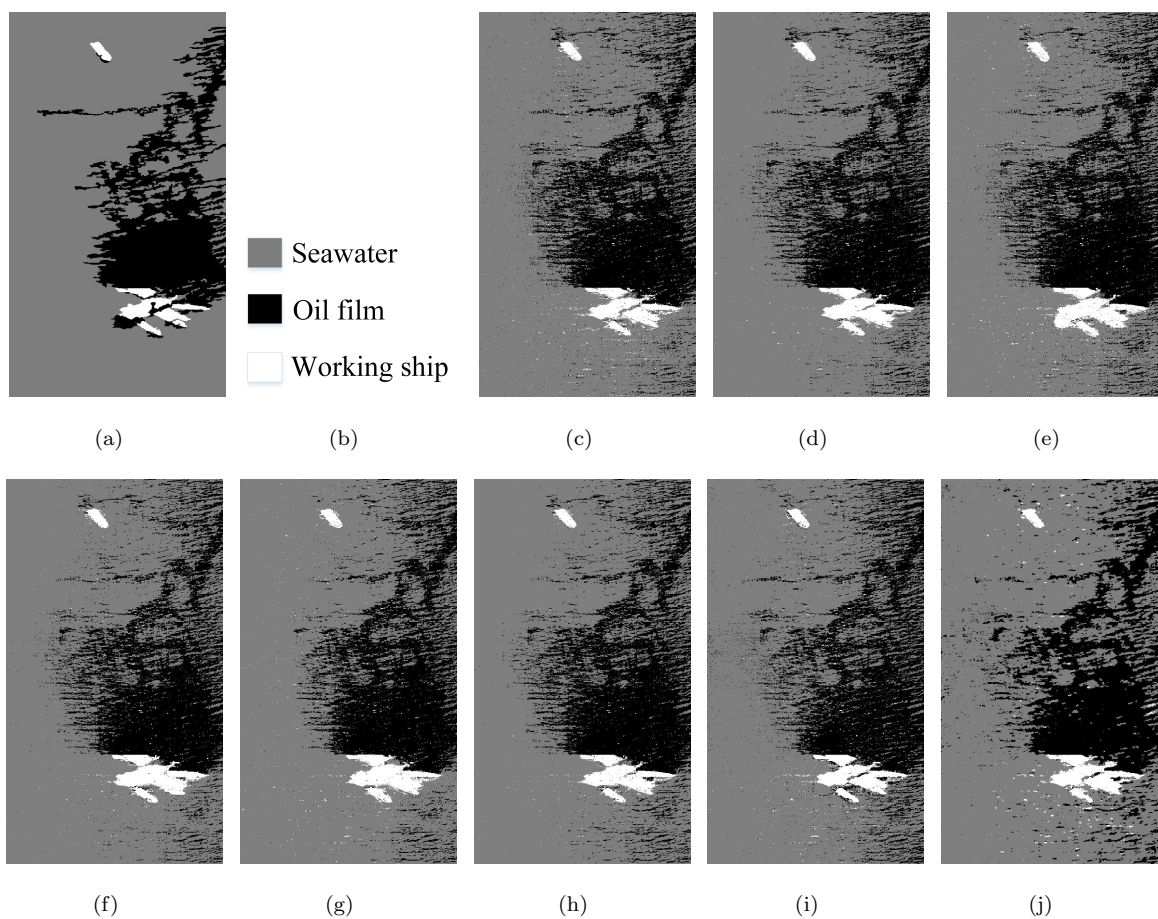


Fig. 16. Classification results obtained by using SVM on different resulting images. (a) Ground truth. (b) Class names. (c) Raw data. (d) Lyzenga *et al.* method [21]. (e) Goodman *et al.* method [22]. (f) Kutser *et al.* method [23]. (g) LRTV method [36]. (h) HyMiNoR method [37]. (i) LRMFBF method [38]. (j) Our method.

## 4. Conclusions

In this work, we have introduced a texture-aware total variation model for removing sun glint. Unlike existing approaches, the sun glint removal problem is first considered as a linear combination of the desired clean image and the sun glint image. We formulate the sun glint removal problem via a variational model, where a texture-aware total variation term is proposed to penalize the induced spectral reflection of the sun glints. Extensive experiments conducted on the simulated and real HSIs demonstrate the effectiveness and superiority of the proposed TATV method in removing sun glint with respect to other state-of-the-art approaches. We have to admit, however, that despite a great improvement for the TATV method, yet there is still room for improvement. The correlation among bands has not taken into consideration. This is a disadvantage that needs to be solved in the future work.

## Acknowledgment

This paper is supported by the Major Program of the National Natural Science Foundation of China (No. 61890962), the National Natural Science Foundation of China (No. 61871179), the National Natural Science Fund of China for International Cooperation and Exchanges (No. 61520106001), the National Science Foundation of Hunan Province (No. 2019JJ50036), the Fund of Key Laboratory of Visual Perception and Artificial Intelligence of Hunan Province (No. 2018TP1013), and the China Scholarship Council.

## References

- [1] J. F. Mustard, M. I. Staid, W. J. Fripp, A semianalytical approach to the calibration of AVIRIS data to reflectance over water: Application in a temperate estuary, *Remote Sens. Environ.* 75 (3) (2001) 335–349 (2001).
- [2] J. Kang, M. Krner, Y. Wang, H. Taubenbck, X. X. Zhu, Building instance classification using street view images, *ISPRS J. Photogramm. Remote Sens.* 145 (2018) 44–59 (2018).
- [3] P. Ghamisi, N. Yokoya, J. Li, W. Liao, S. Liu, J. Plaza, B. Rasti, A. Plaza, Advances in hyper-spectral image and signal processing: A comprehensive overview of the state of the art, *IEEE Geosci. Remote Sens. Mag.* 5 (4) (2017) 37–78 (2017).
- [4] D. Hong, N. Yokoya, N. Ge, J. Chanussot, X. X. Zhu, Learnable manifold alignment (LeMA): A semi-supervised cross-modality learning framework for land cover and land use classification, *ISPRS J. Photogramm. Remote Sens.* 147 (2019) 193–205 (2019).

- [5] A. Plaza, J. A. Benediktsson, J. W. Boardman, J. Brazile, L. Bruzzone, G. Camps-Valls, J. Chanussot, M. Fauvel, P. Gamba, A. Gualtieri, M. Marconcini, J. C. Tilton, G. Trianni, Recent advances in techniques for hyperspectral image processing, *Remote Sens. Environ.* 113 (2009) S110–S122 (2009).
- 305 [6] A. Ibrahim, B. Franz, Z. Ahmad, R. Healy, K. Knobelspiesse, B.-C. Gao, C. Proctor, P.-W. Zhai, Atmospheric correction for hyperspectral ocean color retrieval with application to the hyperspectral imager for the coastal ocean (HICO), *Remote Sens. Environ.* 204 (2018) 60–75 (2018).
- [7] P. Duan, X. Kang, S. Li, P. Ghamisi, J. A. Benediktsson, Fusion of multiple edge-preserving operations for hyperspectral image classification, *IEEE Trans. Geosci. Remote Sens.* 57 (12) (2019) 10336–10349 (2019).
- 310 [8] Y. Liu, G. Gao, Y. Gu, Tensor matched subspace detector for hyperspectral target detection, *IEEE Trans. Geosci. Remote Sens.* 55 (4) (2017) 1967–1974 (2017).
- [9] X. Xu, J. Li, C. Wu, A. Plaza, Regional clustering-based spatial preprocessing for hyperspectral unmixing, *Remote Sens. Environ.* 204 (2018) 333–346 (2018).
- 315 [10] J. D. Hedley, C. Roelfsema, V. Brando, C. Giardino, T. Kutser, S. Phinn, P. J. Mumby, O. Barriero, J. Laporte, B. Koetz, Coral reef applications of Sentinel-2: Coverage, characteristics, bathymetry and benthic mapping with comparison to Landsat 8, *Remote Sens. Environ.* 216 (2018) 598–614 (2018).
- [11] C. Petus, J. Waterhouse, S. Lewis, M. Vacher, D. Tracey, M. Devlin, A flood of information: Using sentinel-3 water colour products to assure continuity in the monitoring of water quality trends in the great barrier reef (australia), *J. Environ. Manage.* 248 (2019) 109–255 (2019).
- 320 [12] C. Roelfsema, E. Kovacs, J. C. Ortiz, N. H. Wolff, D. Callaghan, M. Wettle, M. Ronan, S. M. Hamylton, P. J. Mumby, S. Phinn, Coral reef habitat mapping: A combination of object-based image analysis and ecological modelling, *Remote Sens. Environ.* 208 (2018) 27–41 (2018).
- 325 [13] S. Kay, J. D. Hedley, S. Lavender, Sun glint correction of high and low spatial resolution images of aquatic scenes: a review of methods for visible and near-infrared wavelengths, *Remote Sens.* 1 (4) (2009) 697–730 (2009).
- [14] M. Wang, S. W. Bailey, Correction of sun glint contamination on the seawifs ocean and atmosphere products, *Appl. Opt.* 40 (27) (2001) 4790–4798 (Sep. 2001).
- 330 [15] A. M. Muslim, W. S. Chong, C. D. M. Safuan, I. Khalil, M. S. Hossain, Coral reef mapping of UAV: A comparison of sun glint correction methods, *Remote Sens.* 11 (20) (2019) 2422 (2019).

- [16] F. M. Breon, N. Henriot, Spaceborne observations of ocean glint reflectance and modeling of wave slope distributions, *J. Geophys. Res.* 111 (2) (2006) C06005:1–C06005:10 (2006).
- [17] H. Fukushima, K. Suzuki, L. Li, N. Suzuki, H. Murakami, Improvement of the ADEOS-II/GLI sun-glint algorithm using concomitant microwave scatterometer-derived wind data, *Adv. Space Res.* 43 (6) (2009) 941–947 (2009).
- [18] M. Ottaviani, R. Spurr, K. Stamnes, W. Li, W. Su, W. Wiscombe, Improving the description of sunglint for accurate prediction of remotely sensed radiances, *J. Quant. Spectrosc. Radiat. Transf.* 109 (14) (2008) 2364–2375 (2008).
- [19] E. J. Hochberg, S. Andrefouet, M. R. Tyler, Sea surface correction of high spatial resolution ikonos images to improve bottom mapping in near-shore environments, *IEEE Trans. Geosci. Remote Sens.* 41 (7) (2003) 1724–1729 (2003).
- [20] J. Martin, F. Eugenio, J. Marcello, A. Medina, Automatic sun glint removal of multispectral high-resolution Worldview-2 imagery for retrieving coastal shallow water parameters, *Remote Sens.* 8 (1) (2016) 37 (2016).
- [21] D. R. Lyzenga, N. P. Malinas, F. J. Tanis, Multispectral bathymetry using a simple physically based algorithm, *IEEE Trans. Geosci. Remote Sens.* 44 (8) (2006) 2251–2259 (2006).
- [22] J. A. Goodman, Z. Lee, S. L. Ustin, Influence of atmospheric and sea-surface corrections on retrieval of bottom depth and reflectance using a semi-analytical model: a case study in kaneohe bay, hawaii, *Appl. Opt.* 47 (28) (2008) F1–F11 (Oct. 2008).
- [23] T. Kutser, E. Vahtme, J. Praks, A sun glint correction method for hyperspectral imagery containing areas with non-negligible water leaving NIR signal, *Remote Sens. Environ.* 113 (10) (2009) 2267–2274 (2009).
- [24] K. G. Ruddick, V. D. Cauwer, Y. je Park, G. Moore, Seaborne measurements of near infrared water-leaving reflectance: The similarity spectrum for turbid waters, *Limnol. Oceanogr* 51 (2) (2006) 1167–1179 (Mar. 2006).
- [25] T. Harmel, M. Chami, T. Tormos, N. Reynaud, P.-A. Danis, Sunglint correction of the multispectral instrument (MSI)-SENTINEL-2 imagery over inland and sea waters from SWIR bands, *Remote Sens. Environ.* 204 (2018) 308–321 (2018).
- [26] H. Zhang, W. He, L. Zhang, H. Shen, Q. Yuan, Hyperspectral image restoration using low-rank matrix recovery, *IEEE Trans. Geosci. Remote Sens.* 52 (8) (2014) 4729–4743 (2014).
- [27] J. Kang, Y. Wang, M. Körner, X. X. Zhu, Robust object-based multipass InSAR deformation reconstruction, *IEEE Trans. Geosci. Remote Sens.* 55 (8) (2017) 4239–4251 (2017).

- [28] R. Dian, S. Li, A. Guo, L. Fang, Deep hyperspectral image sharpening, *IEEE Trans. Neural Netw. Learn. Syst.* 29 (11) (2018) 5345–5355 (2018).  
365
- [29] Q. Liu, J. Liu, P. Dong, D. Liang, SGTD: Structure gradient and texture decorrelating regularization for image decomposition, in: *IEEE Int. Conf. Comput. Vis.*, 2013, pp. 1081–1088 (2013).
- [30] P. Duan, X. Kang, S. Li, P. Ghamisi, Noise-robust hyperspectral image classification via multi-scale total variation, *IEEE J. Sel. Topics Appl. Earth Observ. Remote Sens.* 12 (6) (2019) 1948–1962 (2019).  
370
- [31] M. V. Afonso, J. M. R. Sanches, Blind inpainting using  $\ell_0$  and total variation regularization, *IEEE Trans. Image Process.* 24 (7) (2015) 2239–2253 (2015).
- [32] J. Kang, Y. Wang, M. Schmitt, X. X. Zhu, Object-based multipass insar via robust low-rank tensor decomposition, *IEEE Trans. Geosci. Remote Sens.* 56 (6) (2018) 3062–3077 (2018).
- [33] D. Hong, N. Yokoya, J. Chanussot, X. X. Zhu, An augmented linear mixing model to address spectral variability for hyperspectral unmixing, *IEEE Trans. Image Process.* 28 (4) (2019) 1923–1938 (2019).  
375
- [34] D. Hong, N. Yokoya, J. Chanussot, X. X. Zhu, Cospace: Common subspace learning from hyperspectral-multispectral correspondences, *IEEE Trans. Geosci. Remote Sens.* 57 (7) (2019) 4349–4359 (2019).  
380
- [35] Y. Wang, J. Yang, W. Yin, Y. Zhang, A new alternating minimization algorithm for total variation image reconstruction, *SIAM J. Imaging Sciences* 1 (2008) 248–272 (2008).
- [36] W. He, H. Zhang, L. Zhang, H. Shen, Total-variation-regularized low-rank matrix factorization for hyperspectral image restoration, *IEEE Trans. Geosci. Remote Sens.* 54 (1) (2016) 178–188 (2016).  
385
- [37] B. Rasti, P. Ghamisi, J. A. Benediktsson, Hyperspectral mixed gaussian and sparse noise reduction, *IEEE Geosci. Remote Sens. Letters* (2019, doi:10.1109/LGRS.2019.2924344) 1–5 (2019, doi:10.1109/LGRS.2019.2924344).
- [38] Y. Chen, X. Cao, Q. Zhao, D. Meng, Z. Xu, Denoising hyperspectral image with non-i.i.d. noise structure, *IEEE Trans. Cybern.* 48 (3) (2018) 1054–1066 (2018).  
390
- [39] X. Kang, P. Duan, X. Xiang, S. Li, J. A. Benediktsson, Detection and correction of mislabeled training samples for hyperspectral image classification, *IEEE Trans. Geosci. Remote Sens.* 56 (10) (2018) 5673–5686 (2018).
- [40] F. Melgani, L. Bruzzone, Classification of hyperspectral remote sensing images with support vector machines, *IEEE Trans. Geosci. Remote Sens.* 42 (8) (2004) 1778–1790 (Aug. 2004).  
395